ACS OMEGA

http://pubs.acs.org/journal/acsodf

Article

Bismuth Ferrite−Silver Nanowire Flexible Nanocomposites for Room-Temperature Nitrogen Dioxide Sensing

Sanjeev Patil, Sudha Arumugam, and Parasuraman Swaminathan*

Cite This: *ACS Omega* 2024, 9, 28978−28988

Read Online

ABSTRACT: Nitrogen dioxide (NO_2) is a major pollutant, causing acid rain, photochemical smog, and respiratory damage. The annual safe limit is 50 parts per billion (ppb), while concentrations exceeding 1 part per million (ppm) can result in respiratory ailments. Conventionally, n-type metal oxide semiconductors operating at elevated temperatures have been utilized for NO_2 detection. Recently, p-type semiconductors with their hole accumulation layer, rapid recovery post-gas exposure, and good humidity tolerance are being investigated as potential NO_2 sensors, once again working at elevated temperatures. In this work, a room-temperature (27 ± 2 °C) NO_2 sensor is demonstrated by using a nanocomposite based on p-type bismuth ferrite (BFO) nanoparticles and silver nanowires (Ag NWs). This nanocomposite is capable of sensing a NO_2 gas concentration of up to 0.2 ppm. The BFO nanoparticles are synthesized via a sol−gel route followed by sintering at 500 °C to form the crystalline phase. Nanocomposites are obtained by formulating a dispersion of the BFO nanoparticles and Ag NWs, followed by direct writing on both flexible and rigid substrates. The Ag NWs act as the conducting pathway, reducing the overall electrical resistance and thus enabling room-temperature operation. X-ray diffraction, scanning electron microscopy, and surface area studies provide phase information and surface morphology, and the porous nature of the film helps in room-temperature gas adsorption. The current−voltage and gas-sensing behavior are studied to obtain the optimized molar ratio (4:1 BFO/Ag NWs) for the sensor. The sensor deposited on poly(ethylene terephthalate) (PET) also works under a bent condition, indicating good flexibility. Rapid NO_2 sensing was achieved in a BFO−Ag/PET device with response/recovery times of 7/8.5 s and 12/15 s in straight and bent geometries, respectively. Additionally, a good sensitivity of 30 to 60% was achieved for the BFO−Ag/PET device across 100 to 1000 ppb of NO_2. The development of a nanocomposite combining an active sensing element (BFO) and a charge-transport element (Ag NWs) opens up a multitude of other application areas.

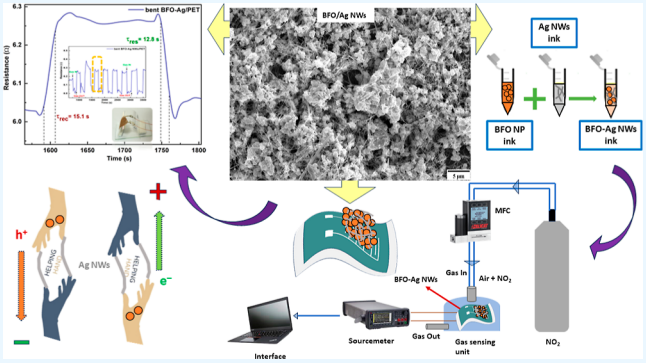

1. INTRODUCTION

Nitrogen dioxide (NO_2) is recognized as one of the most hazardous pollutants in the ever-growing list of materials with health and safety hazards, with automobiles and factories combusting fossil fuels being the primary sources and with secondary contributions coming from chemical industries. While NO_2 poses a serious threat to the environment and ecosystem balance by propagating acid rain and global warming, there is also a serious concern to living beings causing severe respiratory ailments upon prolonged exposure beyond the 0.1 parts per million (ppm) level.[1,2] As a result, it is imperative to develop and install sub-ppm-level NO_2 detection and monitoring systems to ensure safety in commercial, industrial, and residential settings.

Several techniques are currently available for the detection of NO_2 gas, such as phase-shift spectroscopy,[3] chemiluminescence,[4] optical,[5,6] photoacoustic,[7] gas chromatographic,[8] and chemiresistive methods using metal oxide semiconductors (MOSs).[9] While chromatography-based sensors are bulky and high-powered, with poor response times,[10] optical gas sensors are expensive[11] and acoustic gas sensors exhibit poor selectivity.[12] As a result, the most widely studied sensors are MOS-based devices, which work on the principle of resistive sensing; i.e., they detect changes in electrical resistance measured as a function of the target gas type and concentration. MOS sensors have several advantages over others due to their versatility in detecting a variety of target gases (particularly hazardous and flammable), cost-effectiveness, ease of fabrication, abundance, small size, easy integration in devices, and easy maintenance, as well as moderate stability and safety. A plethora of both p-type (such as CuO and NiO)[13] and n-type MOS (ZnO, SnO_2, In_2O_3, TiO_2, and

Received: April 28, 2024
Revised: June 12, 2024
Accepted: June 13, 2024
Published: June 22, 2024

WO_3)-based NO_2 gas sensors[14−18] have been widely studied.[19] However, these primary metal oxides have significant drawbacks such as employing elevated operating temperatures,[20] environmental degradation, poor electrical stability,[21] poor cross selectivity,[22] and declining efficiency in a humid atmosphere.[23] To overcome this, the use of ternary perovskite oxides (such as $BiFeO_3$, $LaFeO_3$,[24,25] $SmFeO_3$,[26] $LnFeO_3$,[27] $YMnO_3$,[28] and $YCoO_3$[29]) has gained traction. These oxides eliminate existing deficiencies with regards to structural instability and oxygen vacancies induced from nonstoichiometry, typically associated otherwise with binary oxides. Their environmental stability also allows operating over a range of temperatures with minimum degradation even in a humid atmosphere.[30] Furthermore, the characteristic oxygen species adsorption on p-type semiconductor metal oxides also enables them to be relatively humidity-resistant to degradation during gas response.[23]

Volatile organic compounds (VOC) sensing using noble-metal-doped bismuth ferrite (BFO) has been reported but an operating temperature of 350 to 450 °C was required, thus highlighting the need for successful detection of sub-ppm NO_2 at room temperature.[30] Additionally, while bulk BFO pellets have been used for sensing, there is a need for flexible conformable devices that enable good sensitivity and rapid response to gas, even in bent geometry. Sr-doped BFO has been reported for NO_2 sensing with an intricate fabrication procedure that involves processing in excess of 20 h as well as high-temperature sintering at 600 °C immediately before sensing measurements.[31] This is not representative of an ambient environment that has humidity present, and the values obtained are synthetically enhanced due to this 600 °C thermal activation acting as an external driving force for sensing, while there is an additional constant operating temperature used for gas sensing from 260 to 500 °C. This highlights the need for NO_2 sensing at room temperature without any heating during sensing measurements. Additionally, there exists scope for improvement in response/recovery times. A room-temperature sensor for NO_2 based on $CH_3NH_3PbI_3$ was reported; however, the perovskite used the lead element which is toxic.[32] Furthermore, the concentration recorded in this work is 1 ppm, while it is imperative to achieve sub-ppm-level detection (0.2 ppm) without the use of toxic chemicals. Moreover, this report used an alumina substrate that is rigid and brittle, therefore unsuitable for flexible applications.

BFO is a unique member of the multiferroic family exhibiting piezoelectric, ferroelectric, and antiferromagnetic behavior simultaneously at room temperature. BFO is a p-type semiconductor with an ABO_3 perovskite structure and an optical band gap ranging from 1.9 to 2.7 eV, depending on stoichiometry and defects during synthesis. It is widely reported as a promising material for multiferroic applications such as magneto-electricity, spintronics, and ferroelectric random access memory, to name a few.[33] Recent studies have discussed BFO ($BiFeO_3$) as a sensor for sulfur dioxide,[34] ammonia,[35] and acetone[36] detection, thus showing the material's promise toward gas-sensing applications. BFO possesses good chemical and thermal stability, optical band gap in the visible light range, and a unique room-temperature multiferroic nature enabling efficient charge separation, all the traits desired in a practical gas-sensing material.[37]

Still, few reports are available that explore the gas-sensing properties of BFO, perhaps due to the relative difficulty of working with and understanding the electronic mechanism behind oxidizing gas sensing using a p-type semiconductor. The few reports that discussed BFO for gas sensing employed doped BFO as the active sensing layer but, more importantly, they all required operating temperatures in the range of 200 to 400 °C.[31,38−40] Specifically for NO_2 sensing, the W-doped BFO study displayed response/recovery times of 80/100 s,[40] whereas the Pd-doped BFO study reported 90/110 s;[38] they displayed the significant limitation of additional heating/operating temperatures up to 270 °C.

Since the reported sensitivity values for pure BFO are low, especially at room temperature, incorporation of noble metals such as gold,[41] platinum,[42] and silver[43] was found to improve its gas-sensing properties. The addition of a noble metal (in this work, silver as part of the composite) creates a heterogeneous interface with the MOS. This leads to improved gas-sensing performance by facilitating efficient charge transfer to the underlying interdigitated electrodes (IDEs). Specifically, silver on account of its chemical stability does not interact with the target gas species, but by forming a Schottky junction with the sensing material (here, BFO), it enhances the response of the sensing material due to efficient charge separation and collection. Furthermore, noble metals act as favorable sites for gas adsorption through their catalytic behavior and coupled with large surface areas provided by high aspect ratio NWs, this allows a remarkably low detection range at room temperature with better sensitivity. While previously discussed reports utilized metal nanoparticles (NPs), metal nanowires (NWs) can provide better enhancement in gas sensing owing to their high aspect ratios, greater adsorption and interaction sites for gas species, and crucially, the capability to electrically link the individual MOS NPs with improved charge-transfer characteristics. Silver NWs (Ag NWs), in particular, exhibit good flexibility, transparency, thermal stability, and conductivity, parameters that can enable the development of efficient flexible sensors. Typical challenges associated with Ag NWs include poor interconnection at NW−NW junctions and poor adhesion, which can be improved by blending with metal oxides, and high surface roughness, which turns out to be beneficial for gas-sensing applications. There are reports utilizing pure Ag NWs and NW-based composites for applications such as flexible touch displays,[44] transparent capacitive touch pads,[45,46] heaters,[47,48] and photodetectors.[49,50] At present, there exists no report on a nanocomposite of BFO and Ag NWs for room-temperature gas sensing, and it is imperative to study the expected enhancement in sensing properties imparted by the NWs.

This paper reports the synthesis of a BFO−Ag NW nanocomposite based on sol−gel-synthesized BFO NPs and commercially obtained Ag NWs for room-temperature (27 ± 2 °C) NO_2 gas sensing. The sensor is capable of sub-ppm NO_2 detection and also works in a bent condition when printed on a flexible substrate such as poly(ethylene terephthalate) (PET). The device is fabricated by direct writing, which is a form of extrusion printing. First, a Ag NP IDE pattern is printed on glass, quartz, and PET substrates. A layer of BFO−Ag NW nanocomposite ink is subsequently printed on top of the IDE. We report on the structural properties of the composite via X-ray diffraction (XRD), scanning electron microscopy (SEM), Raman spectroscopy, and Brunauer, Emmett, and Teller (BET) gas adsorption tests, followed by the electrical (I−V) characterization with and without the target gas (NO_2). The nanocomposite is found to exhibit superior sensitivity along with environmental stability when compared to previously

https://doi.org/10.1021/acsomega.4c04076
ACS Omega 2024, 9, 28978−28988

reported BFO-based studies for NO_2 sensing. We also report a possible mechanism for p-type metal oxide (such as BFO) sensing of oxidizing gases, such as NO_2. This work shows that nanocomposites of Ag NWs with ternary oxides, particularly perovskites, are well-suited for the development of flexible room-temperature (FRT) gas sensors.

2. EXPERIMENTAL DETAILS

Pure $BiFeO_3$ NPs were synthesized by a low-temperature wet chemical sol−gel route by employing bismuth nitrate pentahydrate [$Bi(NO_3)_3{\cdot}5H_2O$] and iron(III) nitrate nonahydrate [$Fe(NO_3)_3{\cdot}9H_2O$] (Alfa Aesar ACS grade 98%) as the precursors with acetic acid (EMPARTA Merck 100%) as the chelating agent. The precursors were taken in an appropriate stoichiometric ratio, with 10% excess bismuth nitrate to compensate for bismuth volatility loss during sintering,[51−53] and dissolved in ethylene glycol followed by mixing and stirring to obtain a homogeneous solution. Addition of the chelating agent was followed by stirring at 60 °C until gelation was observed in the form of a 3D hydrogel network accompanied by a color change to chrome yellow.[53] Further drying was undertaken to obtain $BiFeO_3$ powder that was subsequently sintered at 500 °C for 3 h to obtain crystalline $BiFeO_3$. The BFO−Ag NW composite ink was formulated by mixing the in-house synthesized $BiFeO_3$ NPs with commercial Ag NWs (Dycotec Materials, approximately 96 μm long with an average diameter of 80 nm), both dispersed in isopropyl alcohol (IPA). A 4:1 molar ratio of BFO and Ag NWs was optimized and used for the sensing layer.

For fabricating the gas sensor, PET, glass, and quartz substrates were cleaned by sonicating for 5 min each in acetone, ethanol, IPA, and deionized water in that sequence. PET is the flexible substrate, while glass and quartz were used as the traditional rigid substrates for comparison. Ag NPs (Dycotec Materials DM-SIJ-3200 with a density of 1.5 g cm^{-3} and concentration of 5 mg/mL in IPA dispersion) were used to print IDE patterns onto these substrates using a custom-built direct writer printer (Avay Biosciences Pvt. Ltd.). The IDE patterns contained alternating horizontal electrodes with a spacing of 0.75 mm and line thickness of 1 mm with an overall width of 8.5 mm. Printing was followed by annealing of the IDE patterns at 90 °C for 10 min. The BFO−Ag NW composite ink was printed on top of the IDE pattern, followed by drying at 100 °C for 1 h. The schematic of the inks and the IDE pattern with the printed ink is shown as part of Figure S1 in the Supporting Information file.

The structural analysis of the films was carried out by XRD (Bruker D8 DISCOVER AXS powder diffractometer) with a Cu K_α source of wavelength 0.154 nm. The surface morphology and qualitative stoichiometry were studied using SEM (Thermo Fisher Apreo S) with energy-dispersive spectroscopy (EDS). The surface area of the as-synthesized NPs along with pore diameter was measured using the BET method with nitrogen adsorption at 77 K using adsorption−desorption isotherms obtained from a Micromeritics Model: TriStar II. The UV−vis absorbance spectra were recorded using a Jasco V-570 spectrophotometer. Active vibration modes in pure BFO and BFO−Ag NW nanocomposite were obtained using a confocal Raman spectrometer (WiTEC R 300 Source/Nd/YAG, 532 nm). Electrical contacts were made on the IDEs using silver epoxy (60 °C curing for 10 min) prior to gas sensing.

A custom-built gas-sensing unit was used for recording the sensor response to the NO_2 gas. This setup consists of a glass chamber with sample holder arrangement, leak-proof provisions for gas inlet and exhaust, and leads for electrical measurements, as shown in Figure S1. An Alicat mass flow controller was used to monitor and control the NO_2 gas concentration in the range of 0.1 to 1 ppm. The resistance changes (with and without NO_2 gas) were measured using a Keysight B2901A source meter in the form of two probe $I-V$ characteristics by sweeping voltage from −1 to 1 V. All measurements were recorded at room temperature (i.e., 27 ± 2 °C, with the error bar corresponding to the natural variation in ambient temperature) either in ambient air or in a NO_2 atmosphere (standard NO_2 calibration gas balanced with air). The response and recovery times were calculated as the time elapsed to achieve 90% of maximum resistance change during NO_2 gas flow (adsorption) and the time elapsed to drop to 90% of maximum resistance change after venting the NO_2 gas (desorption), respectively. For testing the response under bent condition, the sensor on the PET substrate was bent at a radius of 7 mm, corresponding to a bending angle measured as 140° and $I-V$ as well as response measurements were carried out in this bent configuration to compare to the results obtained when the sensor was straight.

3. RESULTS AND DISCUSSION

3.1. Structural Characterization. XRD study of pure BFO and the BFO−Ag NW nanocomposite, from Figure 1,

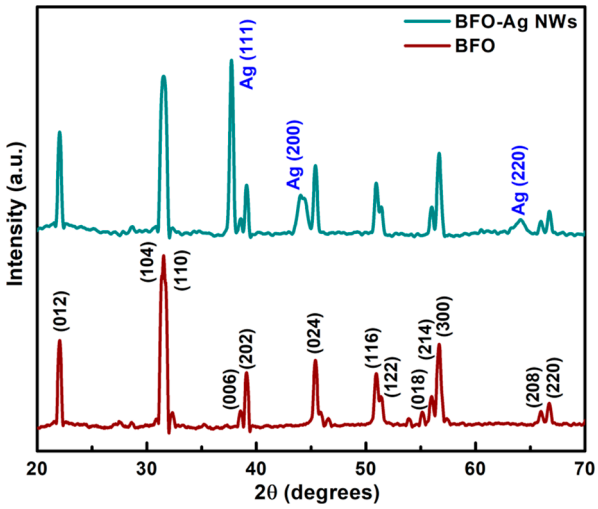

Figure 1. XRD patterns of the as-synthesized pristine BFO and formulated BFO−Ag NW nanocomposite. The peaks correspond to BFO (ICDD number 98-012-3176) and Ag (ICDD number 98-006-2675) and no extra peaks are seen.

shows that the sol−gel synthesis produced phase-pure $BiFeO_3$ with the distorted rhombohedral phase corresponding to ICDD number 98-012-3176.[53] In the nanocomposite, along with BFO, Ag peaks were also identified and assigned to ICDD number 98-006-2675 with there being no evidence of extra peaks belonging to secondary or impurity phases. Thus, the composite formed is a purely physical mixture. An increase in peak intensities for Ag with lowering of BFO peak intensities upon Ag addition has been reported previously.[30,43] This can be explained as the fading of the signal due to greater scattering of X-rays from higher Ag-content BFO samples in addition to

https://doi.org/10.1021/acsomega.4c04076
ACS Omega 2024, 9, 28978−28988

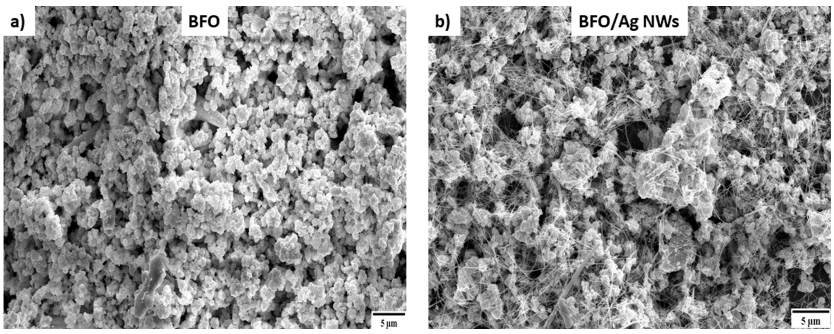

Figure 2. Surface morphology of the (a) pristine BFO NP film and (b) BFO−Ag NW nanocomposite showing the NPs meshed in a network of Ag NWs. The EDS spectra for pure BFO and the nanocomposite are shown in Figure S2.

the difference in the atomic weights between Bi^{3+} (208.98 amu) and Ag^{+} (107.870 amu) ions. Finally, the characteristic length of Ag NWs is around 80 μm, whereas the BFO NPs are 80 nm in diameter; since the Ag NWs can run across and connect several BFO NPs (seen in Figure 2), it is understandable that the longer bridging Ag NWs might diffract more prominently. The average BFO particle size, t_{avg}, was found to be 80 nm as calculated through the Debye−Scherrer equation which is given below

$$t_{avg} = \frac{0.9\lambda}{\beta_{hkl}\cos\theta} \quad (1)$$

where λ is the incident X-ray wavelength, β_{hkl} is the full width at half-maximum (fwhm) for the corresponding diffraction peak (in radians), and θ is Bragg's diffraction angle.

The surface morphologies of pure BFO and the nanocomposite are obtained by SEM and shown in Figure 2a,b, respectively. In the nanocomposite, the Ag NW network meshing with the BFO NPs is clearly visible. A similar morphology was observed in the case of zinc oxide NPs[49] and thermochromic particles[44] meshed in a Ag NW network, which were developed for photodetector and display applications, respectively. The pure BFO NP diameters lie in the 50−80 nm range, similar to values reported in the literature for sol−gel synthesis[53,54] and corresponding well with the crystallite size obtained from XRD data. The EDS plot in Figure S2a qualitatively indicates the presence of Bi, Fe, and O in the appropriate stoichiometric ratios expected for pure BFO, while Figure S2b also shows the presence of Ag in the nanocomposite samples. As evidenced from the SEM images, the BFO−Ag NW nanocomposite films exhibit a highly porous structure that lends itself quite well toward efficient gas adsorption and diffusion.[55]

Structural characterization was further supplemented with Raman spectroscopy. The spectra corresponding to BFO and BFO−Ag NWs are plotted in Figure 3. Three A1-type and seven E-type vibrational modes were observed for pure BFO with a rhombohedral structure corresponding to the *R*3*c* space group.[53] Typically, the A1 modes primarily correspond to longitudinal Bi−O bonds, while the E modes pertain to transverse Fe−O bond vibrations. It is evident from Figure 3 that the intensity of A1 peaks arising from Bi−O is significantly diminished due to the presence of Ag in the nanocomposite. Similar depression in Bi vibrational modes has been previously reported with BFO−Ag,[56] BFO−Co,[57] and BFO−Gd[58] and attributed to the weakening of the Bi−O hybridization due to metal incorporation.

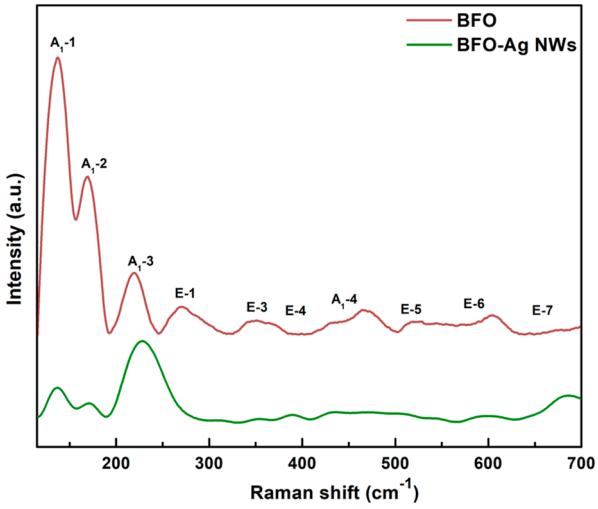

Figure 3. Raman spectra for BFO and BFO−Ag NW films. The pure BFO sample corresponds to the sol−gel-synthesized BFO NPs, while the nanocomposite sample consists of Ag NWs combined with the BFO NPs.

BET results obtained from N_2 adsorption−desorption isotherms yield an average surface area of 4.3 m^2/g for pure BFO NPs. This would be significantly enhanced by the incorporation of Ag NWs to form the composite network. The specific surface area value obtained is higher than previous reported values of 1.6 to 3.1 m^2/g for pure BFO NPs[59,60] which might explain the enhanced gas-sensing property observed in this work. The isotherm obtained from Figure 4 can be categorized as type IV according to IUPAC classification.[61] Type IV isotherms are generally observed for mesoporous structures with the capillary condensation in mesopores responsible for hysteresis-like behavior.[62] The Barrett−Joyner−Halenda (BJH) model was used to get the pore size distribution, indicating a mesoporous structure with a recorded pore size of 3.2 nm that satisfies the 2−50 nm range criteria. Furthermore, the enhanced porous structure in the nanocomposite can be seen from the BJH adsorption and desorption values of pore volume which are 0.03 and 0.04 cm^3/g for the BFO−Ag NW nanocomposite compared to 0.01 and 0.02 cm^3/g for pure BFO NPs, respectively.

3.2. Gas-Sensing Properties. The primary gas-sensing characteristics measured for the BFO−Ag NW composite sensor are its response toward the target gas with changing concentration and the corresponding response and recovery times (t_{res} and t_{rec}). Figure 5 presents the *I*−*V* characteristics of the nanocomposite sensor (on a flexible PET substrate) before

https://doi.org/10.1021/acsomega.4c04076
ACS Omega 2024, 9, 28978−28988

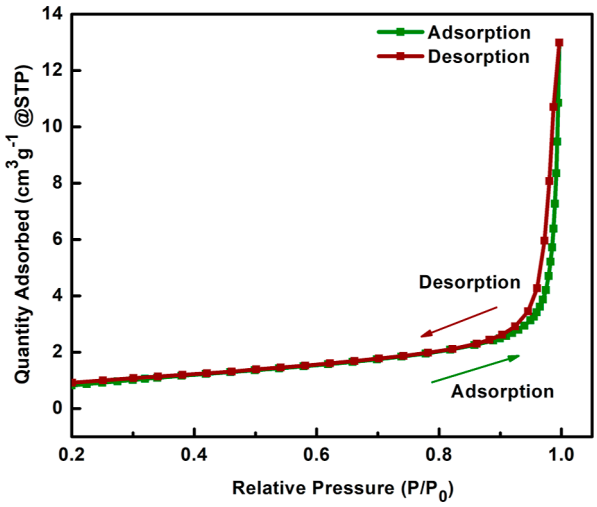

Figure 4. Nitrogen adsorption−desorption plot of BFO NPs for surface area calculation using the BET method. The average surface area calculated was 4.3 m^2/g, significantly higher than reported values in the literature.

and after NO_2 gas exposure at a concentration of 0.2 ppm. Incidentally, pure BFO NPs did not show any response to the gas at room temperature. This is because a high annealing temperature is needed to sinter the particles and form a continuous film. However, this will be incompatible with the flexible PET substrate. The $I-V$ characteristics were measured at room temperature with the voltage sweeping from −1 to +1 V. This low voltage range is due to the good electrical conductivity of the nanocomposite arising from the Ag NW network and can also enable the development of low-powered sensors for practical applications. Measurements were carried out with the PET both in the straight and bent configuration. From Figure 5a,b, it is evident that the device exhibits measurable response to NO_2 at room temperature and that a low applied voltage of 1 V is sufficient for sensing. The sensor shows a comparatively better response in the straight configuration when compared to the bent one, and the overall resistance of the printed nanocomposite layer is lower in the straight configuration. The device was bent with the convex side (consisting of the sensing composite film) up and likely resulted in the stretching of Ag NWs causing disruptions or discontinuities in the network. This is noticed as an increased resistance (lower current) for the bent device geometry in Figure 5 as well as longer response−recovery times, shown in Figure 6. Disruptions in the Ag NW network and an increase in film resistance during bending have been observed earlier with both pure Ag NWs and the Ag NW composite network.[45,48] The increase in current upon NO_2 exposure is due to an increase in the hole concentration at the oxide surface, resulting from the ionosorption of the target oxidizing gas. The $I-V$ data of the sensors fabricated on glass and quartz and tested under similar conditions are shown in Figure S3. These also show well-defined gas response for 0.2 ppm of NO_2, denoted by a measurable increase in current (commensurate with a decrease in the resistance) upon exposure to NO_2 gas which is expected with a p-type semiconductor and oxidizing gas combination.

The gas-sensing behavior on the different substrates, i.e., PET (straight and bent condition), glass, and quartz, was analyzed in order to quantify sensing parameters such as response and recovery times, reproducibility, and stability. Figure 6 shows the gas-sensing response exhibited by the BFO−Ag NW nanocomposite device on PET for repeated flow and purging of the NO_2 gas. The concentration of the gas is maintained at 0.2 ppm during flow. As shown in Figure 6a, the resistance of the BFO−Ag NW composite films decreased by introducing the NO_2 gas and increased back to the original stabilized value when the gas was purged. The magnitude of resistance change observed is approximately 0.2 Ω which translates to a 5 A current signal at a voltage of 1 V, implying superior gas response compared to current state-of-the-art MOS-based NO_2 sensors where the currents are orders of magnitude lower, mainly due to the high resistivity of the MOS. Response time, defined as the time to achieve 90% of the total measured resistance change, was calculated to be 7.0 s, while the recovery time, defined as the time taken to relax back to 10% of the original value, was found to be 8.5 s as seen in Figure 6c, where a single cycle is plotted (the plotted cycle is

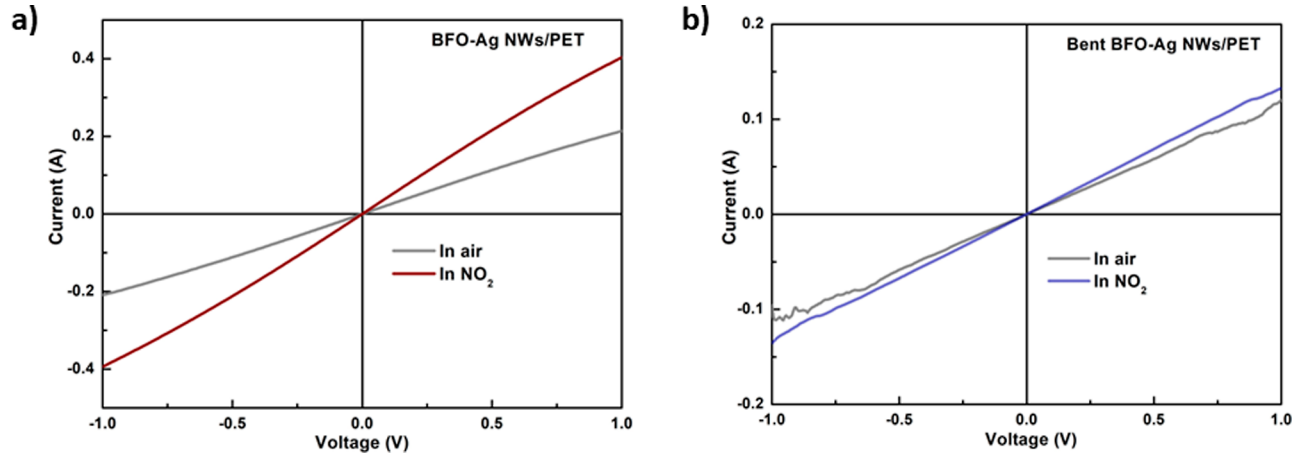

Figure 5. Current−voltage ($I-V$) characteristics for the BFO−Ag NW nanocomposite sensor on PET in (a) straight and (b) bent condition. The $I-V$ plots were measured before (in air) and after 0.2 ppm of NO_2 gas exposure. Both the straight and bent device geometries exhibit and retain Ohmic behavior within the voltage sweep window. While the output current has diminished slightly in the bent configuration, the gas-sensing ability remains unaffected. These devices exhibit superior gas sensing at room temperature and at low applied voltage thereby enabling the development of low-power sensors.

https://doi.org/10.1021/acsomega.4c04076
ACS Omega 2024, 9, 28978−28988

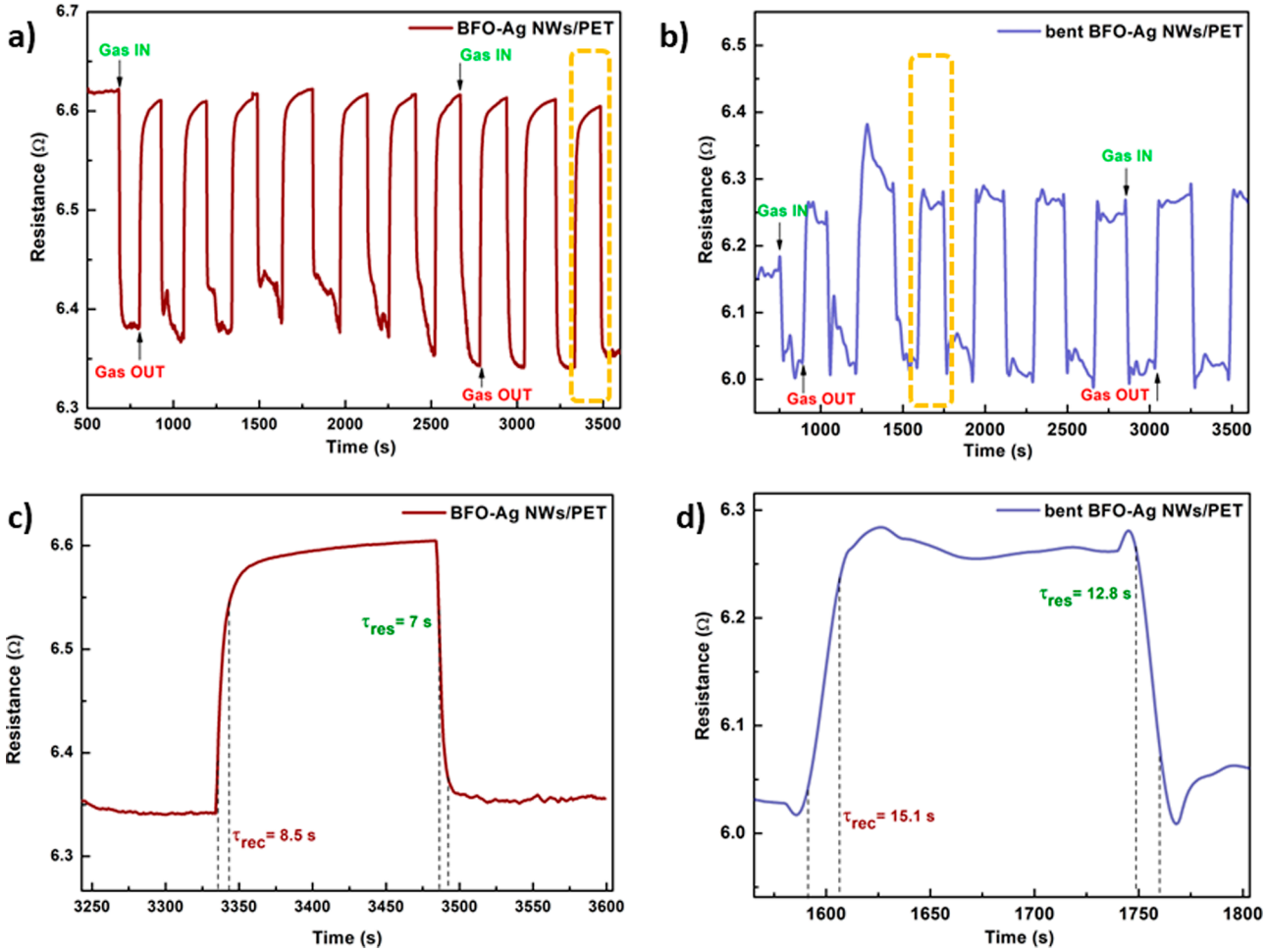

Figure 6. Transient response curves for BFO−Ag NW composites on PET in (a) straight and (b) bent configuration. A single cycle [marked by dotted boxes in (a) and (b)] is expanded for both (c) straight and (d) bent configurations from which the response and recovery times are calculated. All plots are for the exposure of 0.2 ppm of NO_2. Similar plots for the device on glass and quartz substrates are shown in Figure S4.

Table 1. Comparison of BFO-Based Devices for NO_2 Gas Sensing

material/substrate	method of preparation	postprocessing temperature/time	NO_2 concentration	operating temperature	τ_{res}/τ_{rec} (s)	references
Pd−BFO/glass	sol−gel	500 °C/4 h	100 ppm	150 °C	90/110	38
Sr−BFO/TO39	precursor-based modified Pechini method	600 °C/2 h	2 ppm	260 °C	95/280	31
BFO/glass	chemical spray	unannealed	100 ppm	140 °C	80/100	40
W-doped BFO/glass	chemical spray	unannealed	100 ppm	130 °C	70/95	40
BFO−Ag NWs/glass	sol−gel	unannealed	0.2 ppm	room temperature	20.5/21.8	this work
BFO−Ag NWs/quartz					26/44	
BFO−Ag NWs/PET					7/8.5	
BFO−Ag NWs/PET-bent					12.8/15.1	

highlighted by the dotted box in Figure 6a). Similarly, the gas response and recovery times for the bent device were measured as shown in Figure 6b,d (multiple cycles and single cycle, respectively). The response and recovery times in the bent configuration were found to increase to 12.8 and 15.1 s, respectively. The straight device has better response−recovery times when compared to the bent device, which could be attributed to the disrupted network of BFO NPs and Ag NWs in the bent configuration. Gas adsorption and desorption might also be affected in the bent configuration, which can increase the response and recovery times. The sensor response was also obtained for devices on glass and quartz, and these are shown in Figure S4. The response and recovery times on these substrates were measured to be 20.5 and 21.8 s for glass and 26.0 and 44.0 s for quartz, respectively. While these values are higher than those for the PET-based devices reported in this work, they are still faster when compared to values reported for other BFO-based NO_2 sensors while also having the advantage of detecting the target gas at room temperature. The higher response/recovery times on glass and quartz when compared to PET-based devices may be attributed to the slower and more difficult ingress and escape of the NO_2 gas molecules at any discontinuities thus getting stuck in the pores and defect sites on the glass and quartz surfaces.

https://doi.org/10.1021/acsomega.4c04076
ACS Omega 2024, 9, 28978−28988

The room-temperature gas sensitivity and the superior response−recovery times in the present work may be explained by the addition of Ag NWs, the porous morphology of the nanocomposite, and the formation of p-type-metal Schottky heterojunctions at the interfaces between BFO and Ag that improve the electron capture at the BFO surface due to an increased hole accumulation layer (HAL). This results in a better response seen in the faster response/recovery times. From a device point of view, the repeatability of the sensor is established by resistance of the sensor reverting to the baseline value after every cycle, indicating that it is stable enough to detect NO_2 on a consistent basis. To the best of our knowledge, this work represents the first report on the use of BFO NPs with Ag NWs as gas sensors and the precise reason for choosing Ag NWs here was to enhance separation of the charge carriers and thus delay recombination, while also providing an efficient electrical network for the charge carriers to traverse across the sensor providing efficient response when exposed to the target gas. The overall low electrical resistance of the nanocomposite also enables operating at low voltages when compared to pure MOS-based sensors. Table 1 summarizes the response in a quantifiable manner, demonstrating the role played by Ag NWs as efficient enablers in charge transport among the BFO NPs when compared with other systems using pure and doped BFO.

Figure 7 demonstrates the correlation between varying target gas concentration and sensitivity of the FRT sensor, defined as

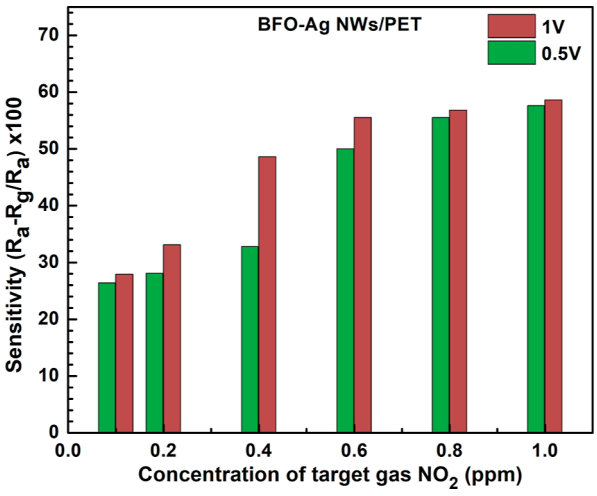

Figure 7. Sensitivity of the flexible BFO−Ag NWs/PET device as a function of the target gas NO_2 concentration. Sensitivity is measured as a ratio of resistance change to the original resistance. R_a is the resistance in air and R_g is the resistance in the presence of NO_2 gas. The device sensitivity was characterized over 0.1 to 1 ppm of NO_2 at two operating voltages of 0.5 and 1 V.

the ratio of resistance change upon gas exposure to the resistance in air. The sensitivity is measured at two voltage values, 0.5 and 1 V. Higher ppm provided a greater change in the measured resistance, seen as a slight increase in the sensitivity values with a successive increase in NO_2 concentration. This behavior is expected as more NO_2 gas molecules interact with the composite surface and adsorbed oxygen anions leading to a wider HAL which manifests as an increased current.[18] Furthermore, the sensor functions appreciably at 0.5 and 1 V, without appreciable degradation in response even at a low voltage of 0.5 V which enables low-powered sensors and easy integration into electronic devices.

To characterize the long-term stability of the fabricated sensors, the devices were tested at room temperature for 0.2 ppm of NO_2 at an interval of 10 days (over a total of 40 days) as shown in Figure 8. The device was stored in an ambient

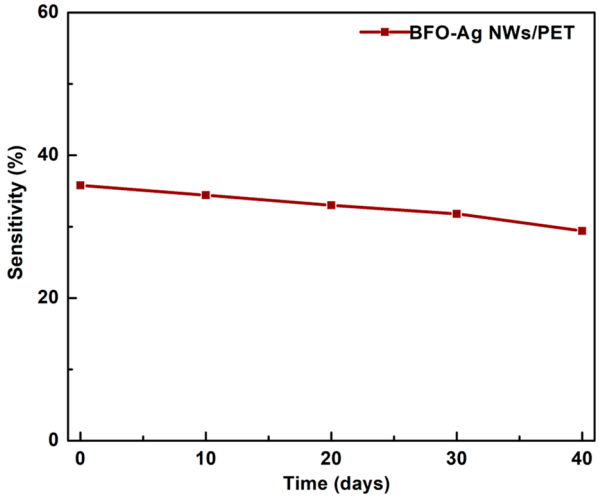

Figure 8. Stability of the flexible BFO−Ag NWs/PET sensor shown as response to NO_2 over a period of 40 days, with measurements once every 10 days. The device was tested at 0.2 ppm of NO_2 at 1 V and stored in an ambient atmosphere between tests.

atmosphere between the tests. It is observed that the sensitivity of the flexible sensor (measured as the ratio of the difference in resistance in ambient and in NO_2 atmospheres to the resistance in an ambient atmosphere) while decreasing to a small extent (∼21% decrease) over a span of 40 days remains significantly measurable over the duration of the stability test. The minor change of the sensitivity may be due to the formation of a moisture layer on the sensor surface or partial surface oxidation of the Ag NWs.

3.3. Gas-Sensing Mechanism. Under ambient conditions, oxygen molecules in the atmosphere adsorb onto the surface of a semiconductor, and owing to oxygen's high electronegativity and electron affinity, they capture electrons from the semiconductor conduction band, thereby forming O_2^- (below 150 °C)[63,64] and O^{2-} adsorbed ions. In the case of a p-type semiconductor, this gives rise to a HAL at the surface and causes a decrease in the electrical resistance.[65,66] Owing to the presence of the Ag NW network in the nanocomposite, a higher number of oxygen molecules get dissociated, through the spillover process, leading to greater adsorption on the BFO surface when compared to pure BFO without the Ag NWs. Thus, there is an increased concentration of surface-adsorbed oxygen, which in turn captures additional electrons (vis-à-vis pure BFO) from the conduction band of the semiconductor surface, thus widening the HAL.[55]

NO_2 being an oxidizing gas (electrophilic species) tends to capture electrons from the materials it comes in contact with. Thus, when NO_2 molecules adsorb onto an oxide surface, they displace the adsorbed oxygen, and this leads to a reduction in the electrons available at the surface with the corollary of an increased hole concentration. This contributes to an increased HAL width at the surface of the sensing films, which manifests in the form of increased current observed in the $I-V$ plot after NO_2 exposure. Hence, a p-type semiconductor exposed to an

https://doi.org/10.1021/acsomega.4c04076
ACS Omega 2024, 9, 28978−28988

oxidizing gas such as NO_2 shows a decrease in resistance (increased current at a constant voltage). The magnitude of the decrease in resistance of the BFO−Ag NW composite material is larger compared to pristine BFO, thereby yielding an enhancement in the sensor response via a form of "chemical sensitization". Upon exposure of NO_2 to the surface of the BFO−Ag NW composite, more gas molecules are adsorbed on the surface due to the greater availability of preferred sites due to the highly porous network structure of BFO−Ag NWs seen in the SEM images and also reflected by the high surface area (4.3 m^2/g) of BFO NPs as revealed by BET analysis in Figure 4. When NO_2 gas interacts with the nanocomposite surface, the gas molecules attract and withdraw electrons from its surface. On account of the higher electron affinity of NO_2 (2.3 eV) compared to the preadsorbed oxygen (0.4 eV), the resistance of the sensing material goes down and eventually will saturate after this adsorption process. The surface accessibility of the material is essential for achieving high sensitivity. In the composite, the efficiency of electron transfer between the NO_2 molecules and the sensing surface improves the sensitivity toward NO_2. Ag NWs also modulate the concentration of the charge carriers in the sensor material that enhances the response via "electronic sensitization". As a result of the metallic Ag NW network in the BFO composite, the rate of the sequential surface reactions is accelerated and reaches saturation rapidly, leading to better response as compared to pure BFO as well as previously reported BFO-based studies. This synergy of a highly reactive sensing surface with Ag NWs enables the composite to detect low concentrations of the target gas with improved response.[30]

Figure S5 depicts the UV−vis absorption spectra and derived Tauc plot giving the optical band gap of the synthesized BFO. Due to the difference in work functions of BFO and Ag, they form a Schottky junction, as shown in Figure 9.[67] This contributes to an enhancement in the gas-sensing response when compared with pure BFO. Li et al. studied the utilization of silver-NP-modified BFO as a chlorine sensor operating at 240 °C.[43] The Schottky junction formed between the Ag and BFO NPs helps in the faster transfer of charge carriers at the interface, improving the response time. Similarly, the Ag can also serve as sites for gas adsorption, improving the overall sensitivity of the device.

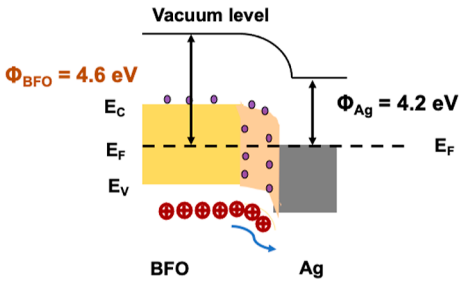

Figure 9. Formation of a Schottky junction at the BFO−Ag NW interface. The junction helps in efficient charge transport, which enhances capture of NO_2 gas by BFO and improves the sensitivity and response time.

In this work, Ag NWs are used to form a composite with BFO instead of the Ag NPs used by Li et al.[43] The higher aspect ratio and surface area of the Ag NWs make them efficient electron harvesters by stimulating electron propagation from BFO to the surface for enhanced gas adsorption. The interaction of NO_2 with this heterojunction results in the formation of NO_3^{2-} upon reacting with the preadsorbed O_2^-. Consequently, an increased hole accumulation and reduced recombination are observed and measured as increased current. Moreover, the Ag NW network helps in the rapid and efficient transfer of charge carriers from BFO. This leads to a larger number of electrons available at the reaction sites which in turn further hastens the capture of electrons by the adsorbed O_2 and NO_2. Hence, the improved effective gas interaction with the sensor surface and gas diffusion kinetics led to a largely improved gas response with a observed reduction in the response and recovery times.[40]

The potential surface reactions in air and NO_2[17] are expanded below in eqs 2−4

In air

$$O_2(g) + e^- \rightarrow O_2^-(ads) \tag{2}$$

In NO_2

$$NO_2 + e^- \rightarrow NO_2^-(ads) \tag{3}$$

$$NO_2 + O_2^-(ads) + 2e^- \rightarrow NO_2^-(ads) + 2O^-(ads) \tag{4}$$

The superior gas-sensing response can primarily be attributed to the synergistic effects of Ag NWs and BFO NPs on the nanocomposite. To summarize, the increased surface area and available sites for gas adsorption and charge transfer, more efficient charge conduction through the device due to the continuous network of Ag NWs connecting the BFO NPs, and the sensitization effects conferred by Ag combine to promote the oxygen ionosorption and increase the chemically adsorbed oxygen molecules on the sensor surface at room temperature under ambient conditions. When NO_2 gas is exposed, the O_2 ions are replaced by NO_2 ions (as shown in eq 4) and the change in resistance due to this adsorption is measured. When the NO_2 gas is removed, the device resistance increases back to the original value.

The sensing performance of the BFO−Ag NW sensor was compared with that of previously reported BFO-based materials for NO_2 sensing and the data is summarized in Table 1. The previous studies were reported with an operating temperature that may restrict potential applications.[40] In contrast, the BFO−Ag NW nanocomposite sensor reported in this study was operated at room temperature with a rapid response time. Moreover, a flexible substrate sensor was also successfully demonstrated, enabling its potential use on irregular surfaces, as well. The inexpensive synthesis and large-scale production-friendly fabrication combined with lower preparation time and absence of any toxic/corrosive chemicals during synthesis add to the appeal of this BFO−Ag NW-based FRT NO_2 sensor.

Additionally, the diffusion of gas molecules into the nanocomposite film is stimulated by the porous structure, providing more active sites and better kinetics for surface chemical reactions. The substantial improvement in gas response for the BFO−Ag NW device compared to previous reports on doped or pristine BFO can also be attributed to the increase in surface area in the nanocomposite on account of the presence of Ag NWs with high aspect ratios providing numerous active sites preferred for adsorption of target gas molecules.[40] From this work, it can be ascertained that our BFO-based composite flexible device is promising for NO_2 gas sensing with room-temperature operation.

https://doi.org/10.1021/acsomega.4c04076
ACS Omega 2024, 9, 28978−28988

4. CONCLUSIONS

We have successfully synthesized BFO−Ag NW-based nanocomposite sensors for room-temperature NO_2 gas sensing. The phase, surface morphology, and elemental composition of pure BFO and the BFO−Ag NW composite were reported. The NO_2 gas-sensing characteristics of the sensors were also investigated in detail. Compared with glass and quartz, the BFO−Ag NW composite on PET substrates exhibited a superior sensitivity with better response/recovery time for straight (7/8.5 s) and bent (12.8/15.1 s) configurations at 0.2 ppm of NO_2 at room temperature in an ambient environment. The enhanced sensing performance can be attributed to the presence of Ag NWs that efficiently separates charge carriers, while simultaneously augmenting the gas adsorption sites with catalytic effect by forming Schottky junctions. This work reports for the first time on BFO-based room-temperature NO_2 sensing, which also demonstrated flexible devices with better response times than the literature. Future work will focus on extending this sensor to other gases, such as CO_2, to understand its selectivity and develop composite gas sensors based on other perovskites and Ag NW composites. Work will also be carried out on the role of humidity and temperature on the performance of the sensor by modifying the gas-sensing chamber.

■ ASSOCIATED CONTENT

Supporting Information

The Supporting Information is available free of charge at https://pubs.acs.org/doi/10.1021/acsomega.4c04076.

Schematic of the gas-sensing setup, EDS spectrum of pure BFO and BFO−Ag NWs composites, *I*−*V* characteristics of BFO−Ag NW composite sensors on glass and quartz substrates, gas-sensing response of BFO−Ag NWs on glass and quartz substrates, and UV−vis absorption spectroscopy with band gap values from the Tauc plot (PDF)

■ AUTHOR INFORMATION

Corresponding Author

Parasuraman Swaminathan − *Electronic Materials and Thin Films Lab, Department of Metallurgical and Materials Engineering and Centre of Excellence in Ceramics Technologies for Futuristic Mobility, IIT Madras, Chennai 600036, India;* orcid.org/0000-0002-9821-3981; Email: swamnthn@iitm.ac.in

Authors

Sanjeev Patil − *Electronic Materials and Thin Films Lab, Department of Metallurgical and Materials Engineering, IIT Madras, Chennai 600036, India*

Sudha Arumugam − *Electronic Materials and Thin Films Lab, Department of Metallurgical and Materials Engineering and Centre of Excellence in Ceramics Technologies for Futuristic Mobility, IIT Madras, Chennai 600036, India*

Complete contact information is available at: https://pubs.acs.org/10.1021/acsomega.4c04076

Author Contributions

S.P. designed the methodology and experiment, synthesized BFO NPs, formulated BFO NP and Ag NW nanocomposite inks, and fabricated the flexible sensor. S.P. carried out structural characterization. A.S. and S.P. performed gas-sensing characterization. S.P. prepared the original draft with A.S.'s contribution. P.S. conceptualized and supervised the study and revised the manuscript.

Notes

The authors declare no competing financial interest.

■ ACKNOWLEDGMENTS

The IIT Madras IoE Research Initiative Project on Materials and Manufacturing for Futuristic Mobility (SB/22-23/1272/MM/ETWO/008702) supported this work. The authors are grateful to Central XRD facility, IIT Madras for XRD measurements. The authors acknowledge the Department of Metallurgical and Materials Engineering, IIT Madras for the SEM images and BET data. The MSRC facility at IIT Madras was utilized for Raman spectroscopy measurements.

■ REFERENCES

(1) Wu, J.; Wu, Z.; Ding, H.; Wei, Y.; Huang, W.; Yang, X.; Li, Z.; Qiu, L.; Wang, X. Flexible, 3D SnS_2/reduced graphene oxide heterostructured NO2 sensor. *Sens. Actuators, B* **2020**, *305*, 127445.

(2) Guarnieri, M.; Balmes, J. R. Outdoor air pollution and asthma. *Lancet* **2014**, *383*, 1581−1592.

(3) Kebabian, P. L.; Wood, E. C.; Herndon, S. C.; Freedman, A. A practical alternative to chemiluminescence-based detection of nitrogen dioxide: Cavity attenuated phase shift spectroscopy. *Environ. Sci. Technol.* **2008**, *42*, 6040−6045.

(4) Zhang, W.; Yang, F.; Xu, J.; Gu, C.; Zhou, K. Sensitive Carbon Monoxide Gas Sensor Based on Chemiluminescence on Nano-Au/Nd_2O_3−$Ca_3Nd_2O_6$: Working Condition Optimization by Response Surface Methodology. *ACS Omega* **2020**, *5*, 20034−20041.

(5) Ashkavand, Z.; Sadeghi, E.; Parvizi, R.; Zare, M. Developed low-temperature anionic 2H-MoS_2/Au sensing layer coated optical fiber gas sensor. *ACS Appl. Mater. Interfaces* **2020**, *12*, 34283−34296.

(6) Casals, O.; Markiewicz, N.; Fabrega, C.; Gràcia, I.; Cané, C.; Wasisto, H. S.; Waag, A.; Prades, J. D. A parts per billion (ppb) sensor for NO_2 with microwatt (μW) power requirements based on micro light plates. *ACS Sens.* **2019**, *4*, 822−826.

(7) Karhu, J.; Hieta, T.; Manoocheri, F.; Vainio, M.; Ikonen, E. LED-based photoacoustic NO_2 sensor with a sub-ppb detection limit. *ACS Sens.* **2021**, *6*, 3303−3307.

(8) Zampolli, S.; Elmi, I.; Stürmann, J.; Nicoletti, S.; Dori, L.; Cardinali, G. Selectivity enhancement of metal oxide gas sensors using a micromachined gas chromatographic column. *Sens. Actuators, B* **2005**, *105*, 400−406.

(9) Chen, X.; Shen, Y.; Zhou, P.; Zhao, S.; Zhong, X.; Li, T.; Han, C.; Wei, D.; Meng, D. NO_2 sensing properties of one-pot-synthesized ZnO nanowires with Pd functionalization. *Sens. Actuators, B* **2019**, *280*, 151−161.

(10) Zampolli, S.; Elmi, I.; Cardinali, G. C.; Masini, L.; Bonafè, F.; Zardi, F. Compact-GC platform: A flexible system integration strategy for a completely microsystems-based gas-chromatograph. *Sens. Actuators, B* **2020**, *305*, 127444.

(11) Xu, H.; Wu, P.; Zhu, C.; Elbaz, A.; Gu, Z. Z. Photonic crystal for gas sensing. *J. Mater. Chem. C* **2013**, *1*, 6087−6098.

(12) Xie, J.; Zhang, L.; Xing, H.; Bai, P.; Liu, B.; Wang, C.; Lei, K.; Wang, H.; Peng, S.; Yang, S. Gas sensing of ordered and disordered structure SiO_2 and their adsorption behavior based on quartz crystal microbalance. *Sens. Actuators, B* **2020**, *305*, 127479.

(13) Bai, H.; Feng, C.; Guo, H.; Li, X.; Liu, W.; Feng, Y.; Liu, K.; Chen, D.; Zheng, Y.; Guo, F. UV-activated CuO nanospheres modified with rGO nanosheets for ppb-level detection of NO_2 gas at room temperature. *Sens. Actuators, B* **2023**, *393*, 134195.

(14) Wang, Z.; Han, T.; Fei, T.; Liu, S.; Zhang, T. Investigation of microstructure effect on NO_2 sensors based on SnO_2 nanoparticles/reduced graphene oxide hybrids. *ACS Appl. Mater. Interfaces* **2018**, *10*, 41773−41783.

(15) Roso, S.; Degler, D.; Llobet, E.; Barsan, N.; Urakawa, A. Temperature-dependent NO_2 sensing mechanisms over indium oxide. *ACS Sens.* **2017**, *2*, 1272−1277.
(16) Li, Z.; Zhang, Y.; Zhang, H.; Jiang, Y.; Yi, J. Superior NO_2 sensing of MOF-derived indium-doped ZnO porous hollow cages. *ACS Appl. Mater. Interfaces* **2020**, *12*, 37489−37498.
(17) Siriwalai, M.; Punginsang, M.; Inyawilert, K.; Wisitsoraat, A.; Tuantranont, A.; Liewhiran, C. Flame-Spray-Synthesized La_2O_3-Loaded WO_3 Nanoparticle Films for NO_2 Sensing. *ACS Appl. Nano Mater.* **2023**, *6*, 995−1008.
(18) Ueda, T.; Boehme, I.; Hyodo, T.; Shimizu, Y.; Weimar, U.; Barsan, N. Effects of gas adsorption properties of an Au-loaded porous In_2O_3 sensor on NO_2-sensing properties. *ACS Sens.* **2021**, *6*, 4019−4028.
(19) Tamvakos, A.; Korir, K.; Tamvakos, D.; Calestani, D.; Cicero, G.; Pullini, D. NO_2 gas sensing mechanism of ZnO thin-film transducers: physical experiment and theoretical correlation study. *ACS Sens.* **2016**, *1*, 406−412.
(20) Tie, Y.; Ma, S.; Pei, S.; Zhang, Q.; Zhu, K.; Zhang, R.; Xu, X.; Han, T.; Liu, W. Pr doped $BiFeO_3$ hollow nanofibers via electrospinning method as a formaldehyde sensor. *Sens. Actuators, B* **2020**, *308*, 127689.
(21) Zeng, H.; Takahashi, T.; Kanai, M.; Zhang, G.; He, Y.; Nagashima, K.; Yanagida, T. Long-term stability of oxide nanowire sensors via heavily doped oxide contact. *ACS Sens.* **2017**, *2*, 1854−1859.
(22) Comini, E.; Baratto, C.; Faglia, G.; Ferroni, M.; Vomiero, A.; Sberveglieri, G. Quasi-one dimensional metal oxide semiconductors: Preparation, characterization and application as chemical sensors. *Prog. Mater. Sci.* **2009**, *54*, 1−67.
(23) Kim, H.-J.; Lee, J.-H. Highly sensitive and selective gas sensors using p-type oxide semiconductors: Overview. *Sens. Actuators, B* **2014**, *192*, 607−627.
(24) Bai, S.; Shi, B.; Ma, L.; Yang, P.; Liu, Z.; Li, D.; Chen, A. Synthesis of $LaFeO_3$ catalytic materials and their sensing properties. *Sci. China, Ser. B: Chem.* **2009**, *52*, 2106−2113.
(25) Sharma, N.; Kushwaha, H. S.; Sharma, S.; Sachdev, K. Fabrication of $LaFeO_3$ and rGO-$LaFeO_3$ microspheres based gas sensors for detection of NO_2 and CO. *RSC Adv.* **2020**, *10*, 1297−1308.
(26) Huang, H.-T.; Zhang, W.-L.; Zhang, X.-D.; Guo, X. NO_2 sensing properties of $SmFeO_3$ porous hollow microspheres. *Sens. Actuators, B* **2018**, *265*, 443−451.
(27) Thirumalairajan, S.; Girija, K.; Mastelaro, V. R.; Ponpandian, N. Surface morphology-dependent room-temperature $LaFeO_3$ nanostructure thin films as selective NO_2 gas sensor prepared by radio frequency magnetron sputtering. *ACS Appl. Mater. Interfaces* **2014**, *6*, 13917−13927.
(28) Addabbo, T.; Bertocci, F.; Fort, A.; Gregorkiewitz, M.; Mugnaini, M.; Spinicci, R.; Vignoli, V. Gas sensing properties of $YMnO_3$ based materials for the detection of NO_x and CO. *Sens. Actuators, B* **2017**, *244*, 1054−1070.
(29) Addabbo, T.; Bertocci, F.; Fort, A.; Gregorkiewitz, M.; Mugnaini, M.; Spinicci, R.; Vignoli, V. Gas sensing properties and modeling of $YCoO_3$ based perovskite materials. *Sens. Actuators, B* **2015**, *221*, 1137−1155.
(30) Neogi, S.; Ghosh, R. Behavioral remodeling of perovskite $BiFeO_3$ by Ag-doping strategies for enhanced and ppb level acetone sensing performance: An advanced enlightenment for selectivity and sensing mechanism. *Appl. Mater. Today* **2022**, *29*, 101611.
(31) Dmonte, D. J.; Bhardwaj, A.; Wilhelm, M.; Fischer, T.; Kuřitka, I.; Mathur, S. Sub PPM Detection of NO_2 Using Strontium Doped Bismuth Ferrite Nanostructures. *Micromachines* **2023**, *14*, 644.
(32) Fu, X.; Jiao, S.; Dong, N.; Lian, G.; Zhao, T.; Lv, S.; Wang, Q.; Cui, D. A CH_3 NH_3 PbI_3 film for a room-temperature NO_2 gas sensor with quick response and high selectivity. *RSC Adv.* **2018**, *8*, 390−395.
(33) Zhang, Q.; Sando, D.; Nagarajan, V. Chemical route derived bismuth ferrite thin films and nanomaterials. *J. Mater. Chem. C* **2016**, *4*, 4092−4124.
(34) Das, S.; Rana, S.; Mursalin, S. M.; Rana, P.; Sen, A. Sonochemically prepared nanosized $BiFeO_3$ as novel SO_2 sensor. *Sens. Actuators, B* **2015**, *218*, 122−127.
(35) Maricar, S. M. M. S.; Sastikumar, D.; Vanga, P. R.; Ashok, M. $BiFeO_3$ clad modified fiber optic gas sensor for room temperature applications. *Mater. Today: Proc.* **2021**, *39*, 245−249.
(36) Chakraborty, S.; Pal, M. Highly selective and stable acetone sensor based on chemically prepared bismuth ferrite nanoparticles. *J. Alloys Compd.* **2019**, *787*, 1204−1211.
(37) Wang, J.; Wei, Y.; Zhang, J.; Ji, L.; Huang, Y.; Chen, Z. Synthesis of pure-phase $BiFeO_3$ nanopowder by nitric acid-assisted gel. *Mater. Lett.* **2014**, *124*, 242−244.
(38) Waghmare, S. D.; Raut, S. D.; Ghule, B. G.; Jadhav, V. V.; Shaikh, S. F.; Al-Enizi, A. M.; Ubaidullah, M.; Nafady, A.; Thamer, B. M.; Mane, R. S. Pristine and palladium-doped perovskite bismuth ferrites and their nitrogen dioxide gas sensor studies. *J. King Saud Univ., Sci.* **2020**, *32*, 3125−3130.
(39) Li, X.; Zhang, L.; Luo, N.; Chen, J.; Cheng, J.; Ren, W.; Xu, J. Enhanced H_2S sensing performance of $BiFeO_3$ based MEMS gas sensor with corona poling. *Sens. Actuators, B* **2022**, *358*, 131477.
(40) Waghmare, S. D.; Jadhav, V. V.; Shaikh, S. F.; Mane, R. S.; Rhee, J. H.; O'Dwyer, C. Sprayed tungsten-doped and undoped bismuth ferrite nanostructured films for reducing and oxidizing gas sensor applications. *Sens. Actuators, A* **2018**, *271*, 37−43.
(41) Della Gaspera, E.; Guglielmi, M.; Martucci, A.; Giancaterini, L.; Cantalini, C. Enhanced optical and electrical gas sensing response of sol−gel based NiO−Au and ZnO−Au nanostructured thin films. *Sens. Actuators, B* **2012**, *164*, 54−63.
(42) Fu, J.; Zhao, C.; Zhang, J.; Peng, Y.; Xie, E. Enhanced gas sensing performance of electrospun Pt-functionalized NiO nanotubes with chemical and electronic sensitization. *ACS Appl. Mater. Interfaces* **2013**, *5*, 7410−7416.
(43) Li, Q.; Zhang, W.; Wang, C.; Ma, J.; Ning, L.; Fan, H. Ag modified bismuth ferrite nanospheres as a chlorine gas sensor. *RSC Adv.* **2018**, *8*, 33156−33163.
(44) Nair, N. M.; Khanra, I.; Ray, D.; Swaminathan, P. Silver nanowire-based printable electrothermochromic ink for flexible touch-display applications. *ACS Appl. Mater. Interfaces* **2021**, *13*, 34550−34560.
(45) Nair, N. M.; Daniel, K.; Vadali, S. C.; Ray, D.; Swaminathan, P. Direct writing of silver nanowire-based ink for flexible transparent capacitive touch pad. *Flexible Printed Electron.* **2019**, *4*, 045001.
(46) Sharma, N.; Nair, N. M.; Nagasarvari, G.; Ray, D.; Swaminathan, P. A review of silver nanowire-based composites for flexible electronic applications. *Flexible Printed Electron.* **2022**, *7*, 014009.
(47) Bhargavi, T.; Nair, N. M.; Belavadi, A.; Swaminathan, P. Fabrication of a Printed Heater Using a Composite of Silver Nanowires and Neutral PEDOT:PSS. *IEEE J. Flex. Electron.* **2023**, *2*, 395−401.
(48) Nair, N. M.; Pakkathillam, J. K.; Kumar, K.; Arunachalam, K.; Ray, D.; Swaminathan, P. Printable silver nanowire and PEDOT: PSS nanocomposite ink for flexible transparent conducting applications. *ACS Appl. Electron. Mater.* **2020**, *2*, 1000−1010.
(49) M Nair, N.; Jahanara, M. M.; Ray, D.; Swaminathan, P. Photoresponse of a printed transparent silver nanowire-zinc oxide nanocomposite. *Flexible Printed Electron.* **2021**, *6*, 045004.
(50) Solly, M. M.; Sharma, N.; Swaminathan, P. A Transparent Photodetector Based on a Composite of Silver and Tungsten Oxide Nanowires. *IEEE J. Flex. Electron.* **2023**, *2*, 421−428.
(51) Hardy, A.; Gielis, S.; Van den Rul, H.; D'Haen, J.; Van Bael, M.; Mullens, J. Effects of precursor chemistry and thermal treatment conditions on obtaining phase pure bismuth ferrite from aqueous gel precursors. *J. Eur. Ceram. Soc.* **2009**, *29*, 3007−3013.
(52) Albino, G. M.; Perales-Pérez, O.; Renteria, B.; Galvez, M.; Guinel, M. J. *Tuning Of Magnetic Properties In Cobalt-Doped Nanocrystalline Bismuth Ferrite*; MRS Online Proceedings Library (OPL), 2011; p 1368.

(53) Patil, S.; Swaminathan, P. Precursor-based bismuth ferrite ink for direct writing. *Mater. Lett.* **2023**, *343*, 134390.
(54) Amdouni, W.; Fricaudet, M.; Otoničar, M.; Garcia, V.; Fusil, S.; Kreisel, J.; Maghraoui-Meherzi, H.; Dkhil, B. $BiFeO_3$ Nanoparticles: The "Holy-Grail" of Piezo-Photo-Catalysts? *Adv. Mater.* **2023**, *35*, 2301841.
(55) Li, Z.; Li, H.; Wu, Z.; Wang, M.; Luo, J.; Torun, H.; Hu, P.; Yang, C.; Grundmann, M.; Liu, X.; et al. Advances in designs and mechanisms of semiconducting metal oxide nanostructures for high-precision gas sensors operated at room temperature. *Mater. Horiz.* **2019**, *6*, 470−506.
(56) Camacho-Escobar, L.; Palma-Goyes, R. E.; Ortiz-Landeros, J.; Romero-Ibarra, I.; Gamba-Vásquez, O. A.; Vazquez-Arenas, J. Unraveling the structural and composition properties associated with the enhancement of the photocatalytic activity under visible light of $Ag_2O/BiFeO_3$-Ag synthesized by microwave-assisted hydrothermal method. *Appl. Surf. Sci.* **2020**, *521*, 146357.
(57) Wang, S.; Feng, Y.; Liu, W.; Yu, D.; Li, D. Effects of Co doping on electronic structure and electric/magnetic properties of $La_{0.1}$ $Bi_{0.9}$ FeO_3 ceramics. *Sci. China: Phys., Mech. Astron.* **2013**, *56*, 1861−1865.
(58) Guo, R.; Fang, L.; Dong, W.; Zheng, F.; Shen, M. Enhanced photocatalytic activity and ferromagnetism in Gd doped $BiFeO_3$ nanoparticles. *J. Phys. Chem. C* **2010**, *114*, 21390−21396.
(59) Mhamad, S. A.; Ali, A. A.; Mohtar, S. S.; Aziz, F.; Aziz, M.; Jaafar, J.; Yusof, N.; Wan Salleh, W. N.; Ismail, A. F.; Chandren, S. Synthesis of bismuth ferrite by sol-gel auto combustion method: Impact of citric acid concentration on its physicochemical properties. *Mater. Chem. Phys.* **2022**, *282*, 125983.
(60) Yakout, S. M.; Youssef, A.; Wahba, M. A.; Sharmoukh, W.; El Sayed, A.; Khalil, M. S. Superior ferromagnetic and electrical properties: High purity multiferroic $Bi_{0.98}M_{0.02}FeO_3$ (M= La, Pr, Gd) compositions. *J. Magn. Magn. Mater.* **2022**, *561*, 169751.
(61) Lowell, S.; Shields, J. E.; Thomas, M. A.; Thommes, M. *Characterization of Porous Solids And Powders: Surface Area, Pore Size And Density*; Springer Science & Business Media, 2006; p 16.
(62) Soltani, T.; Lee, B.-K. Novel and facile synthesis of Ba-doped $BiFeO_3$ nanoparticles and enhancement of their magnetic and photocatalytic activities for complete degradation of benzene in aqueous solution. *J. Hazard. Mater.* **2016**, *316*, 122−133.
(63) Wang, Y.; Gao, R.; Zhao, H.; Li, J.; Zhang, R.; Wang, Y.; Zhou, Y. Oxygen vacancy-rich ZnO nanorods-based MEMS sensors for swift trace ethanol recognition. *J. Am. Ceram. Soc.* **2023**, *106*, 1050−1061.
(64) Zhou, Y.; Hu, Z.; Zhao, H.; Wang, Y.; Li, J.; Zou, C. Two-dimensional black phosphorus/tin oxide heterojunctions for high-performance chemiresistive H2S sensing. *Anal. Chim. Acta* **2023**, *1245*, 340825.
(65) Wolkenstein, T. *Electronic Processes On Semiconductor Surfaces During Chemisorption*; Springer Science & Business Media, 2012.
(66) Dong, G.; Fan, H.; Tian, H.; Fang, J.; Li, Q. Gas-sensing and electrical properties of perovskite structure p-type barium-substituted bismuth ferrite. *RSC Adv.* **2015**, *5*, 29618−29623.
(67) Chen, Y.-C.; Zheng, F.-C.; Min, Y.-L.; Wang, T.; Zhang, Y.-G.; Wang, Y.-X. Facile procedure to synthesize highly crystalline Ag/NiO nanocomposite microspheres and their photocatalytic activity. *J. Mater. Sci.: Mater. Electron.* **2012**, *23*, 1592−1598.

https://doi.org/10.1021/acsomega.4c04076
ACS Omega 2024, 9, 28978−28988